



ELSEVIER

Available online at www.sciencedirect.com

SCIENCE @ DIRECT®

Comput. Methods Appl. Mech. Engrg. 192 (2003) 3569–3584

**Computer methods
in applied
mechanics and
engineering**

www.elsevier.com/locate/cma

Multi-potential based discontinuous bifurcation model for jointed rock masses and its application

Weiyuan Zhou *, Yuangao Liu, Jidong Zhao

Department of Hydraulic Engineering, Tsinghua University, Beijing 100084, PR China

Received 30 October 2001; received in revised form 10 October 2002; accepted 8 May 2003

Abstract

Based on the localization mechanism of jointed rock masses, damage localization in jointed rock masses can be treated in terms of discontinuous bifurcation. The discontinuous bifurcation model for jointed rock masses in the framework of multi-potential theory is presented in this paper. A numerical method is used to obtain the solution of the eigenvalue problem resulting from the bifurcation model. Consideration of elements embedded with discontinuous deformation mode is made and corresponding codes are incorporated into standard FEM programs thus enabling the applicability of the programs for localization problems. With the aid of the enhanced FEM program, localization bands, i.e., dominant cracking bands, in specimens under tension or compression are simulated numerically by using the proposed model. Numerical results show different localization bands in distinct load cases. To demonstrate the potential application of this program, analysis of Xiluodu arch dam which is one of the largest arch dams in southwest China, serves as an example of engineering cases. The results of Xiluodu arch dam from numerical analysis and physical modeling test are compared and coincided very well with each other.

© 2003 Elsevier B.V. All rights reserved.

Keywords: Multi-potential; Localization; Discontinuous bifurcation; Jointed rock masses

1. Introduction

Under compression or shearing tests, damage localization is the onset of the failure process in jointed rock masses. The nature of localization phenomena in materials can be characterized as the abrupt change of the deformations within the materials. The localization in elasto-plastic materials usually develops into a narrow band, i.e., localization band. The abrupt change of the deformations actually may appear across interfaces between the localization band and the elastic unloading regions. The interface here usually is known as a singular surface. According to Rudnicki and Rice [15] and Hill and Hutchinson [4], jump of deformation across the singular surface can be considered as a discontinuous bifurcation problem. It is worth noting that the abrupt changes across the singular surface include not only the rate of deformation

* Corresponding author.

E-mail addresses: zhouwy@mail.tsinghua.edu.cn (W. Zhou), liuyuangao98@mails.tsinghua.edu.cn (Y. Liu), zhaojd97@mails.tsinghua.edu.cn (J. Zhao).

gradient but also the rate of deformation. On the basis of analyzing the characteristic tangent stiffness modulus tensor, Ottosen and Runesson [13] obtained the explicit analytical solutions for critical bifurcation directions and corresponding hardening modulus according to spectral analysis of the eigenvalue problem of tensors. Ortiz [11] presented an analytical method for the localization analysis of materials such as concrete and a numerical method to compute characteristic directions of localization bands.

Because of widely distributed microcracks or other microstructures, the failure of jointed rock masses will largely depend on the propagation and distribution of these cracks or microstructures. Under different loading, fractures emerge in different cracking surfaces in the rock mass, and the ultimate failure is usually presented with localization bands. The localizing process of rock masses can approximately be divided into four steps: linear elastic, nonlinear elastic hardening, stress dropping and strain softening, which correspond to the micromechanisms of elastic deformation, stable propagation, unstable propagation and nucleation of microcracks respectively. In large structures built on rock foundations, the deformation, propagation and coalescence of microcracks can usually lead to onset of the dominant cracking band and finally result in the failure of structures.

The volumetric strain of geo-materials, such as rocks and soils, can be caused not only by three-dimensional compression, but also by shearing. In the same way, the shear strain can be caused not only by shearing, but also by hydrostatic pressure. To describe the complex deformation characters of soils, double yield surface theory was presented firstly by Prevost and Hoeg [14], Lade [7] and Seiki Ohmaki [16] and so on. Later, the concepts of partial yield surface and multiple yield surface were introduced by Shen Zhujiang [17] and Yin Zongze [21]. Yang Guanghua [20] presented a generalized potential theory or multi-potential theory for soils with the direct coordinate transformation method in terms of mathematics.

In order to find the deformation mode in regions with highly localized strains, finite elements with embedded discontinuities was originally presented by Ortiz et al. [12]. Following their pioneering work, elements with embedded discontinuities were proposed by large numbers of researchers, such as Belytschko et al. [1], Fish and Belytschko [3], Dvorkin et al. [2], Klisinski et al. [6], Simo et al. [19], Larsson and Runesson [8], Simo and Oliver [18], Oliver [10], Larsson and Runesson [9] and so on. Jirásek [5] gave a comparative study on finite elements with embedded discontinuities.

In this paper, based on micromechanisms of localization phenomena of jointed rock masses, damage localization in jointed rock masses is treated as discontinuous bifurcation. Bifurcation model for jointed rock masses based on multi-potential theory is presented. In order to obtain the solution of the eigenvalue problem resulting from this model, the nonlinear programming method is used in FEM to obtain the numerical results. In order to cope with localization, elements embedded with discontinuous deformations are incorporated into standard FEM program. Localizations of corresponding specimens are simulated with this enhanced FEM programs. Xiluodu arch dam serves as an example to simulate the failure behaviors of structures with the proposed model.

2. Multi-potential theory for jointed rock masses

2.1. Multi-potential theory

Jointed rock masses exhibit distinct mechanical behaviors because of widely distributed microcracks, microdefects or voids in them. To describe the mechanical behaviors taking into account of the influence caused by the microstructure, namely microcracks, microdefects or voids, multi-potential theory is suggested to simulate their mechanical behavior appropriately. According to classical elasto-plastic theory, the total strain increment can be divided into two parts, elastic strain increment and plastic strain increment, i.e.,

$$d\varepsilon_{ij} = d\varepsilon_{ij}^e + d\varepsilon_{ij}^p. \quad (1)$$

The elastic strain increment satisfies the elastic constitutive relationship,

$$d\sigma_{ij} = D_{ijkl}^e d\varepsilon_{kl}^e \tag{2}$$

in which D_{ijkl}^e is the elastic stiffness tensor. Substituting Eq. (2) to Eq. (1),

$$d\sigma_{ij} = D_{ijkl}^e (d\varepsilon_{kl} - d\varepsilon_{kl}^p). \tag{3}$$

According to symmetry of incremental stress tensor $d\sigma_{ij}$ and incremental strain tensor $d\varepsilon_{ij}$, three principal components of the incremental strain tensor, $d\varepsilon_i^p$ ($i = 1, 2, 3$) can be dealt as three components of a 3-D vector $d\varepsilon^p$. They can be formulated as the sum of three linear independent vectors. These vectors can be chosen as the linear independent gradients of three potential functions written as φ_i ($i = 1, 2, 3$). Then these principal components of the incremental strain tensor can be written as:

$$d\varepsilon_i^p = \sum_{k=1}^3 d\lambda_k \cdot \frac{\partial \varphi_k}{\partial \sigma_i}. \tag{4}$$

The generalized constitutive relationship can be derived from the last equation with direct coordinates transformation method as following:

$$d\varepsilon_{ij}^p = \sum_{k=1}^3 d\lambda_k \cdot \frac{\partial \varphi_k}{\partial \sigma_{ij}}. \tag{5}$$

By substituting Eq. (5) into Eq. (3), the elasto-plastic constitutive relationship as follows can be obtained as:

$$d\sigma_{ij} = D_{ijkl}^e (d\varepsilon_{kl} - d\varepsilon_{kl}^p) = D_{ijkl}^e \left(d\varepsilon_{kl} - \sum_{m=1}^3 d\lambda_m \frac{\partial \varphi_m}{\partial \sigma_{kl}} \right). \tag{6}$$

The hardening law of the yield surface is chosen as,

$$\psi_k(\sigma_{ij}, H) = 0 \quad (k = 1, 2, 3). \tag{7}$$

The parameters $d\lambda_m$ in Eq. (6) can be computed from the requirement of consistency as follows:

$$d\psi_k = \frac{\partial \psi_k}{\partial \sigma_{ij}} d\sigma_{ij} + \frac{\partial \psi_k}{\partial H} dH = 0 \quad (k = 1, 2, 3), \tag{8}$$

$$d\lambda_m = A_{mn}^{-1} \frac{\partial \psi_n}{\partial \sigma_{ij}} D_{ijkl}^e d\varepsilon_{kl}. \tag{9}$$

Here,

$$A_{mn} = -\frac{\partial \psi_m}{\partial H} \frac{\partial H}{\partial \varepsilon_{ij}^p} \frac{\partial \varphi_n}{\partial \sigma_{ij}} + \frac{\partial \psi_m}{\partial \sigma_{ij}} D_{ijkl}^e \frac{\partial \varphi_n}{\partial \sigma_{kl}},$$

H is hardening parameter depending on the work hardening law.

Hence the incremental stress–strain relationship

$$D_{ijkl} = \begin{cases} D_{ijkl}^e & \text{Elastic,} \\ D_{ijkl}^e - D_{ijqr}^e \frac{\partial \varphi_m}{\partial \sigma_{qr}} A_{mn}^{-1} \frac{\partial \psi_n}{\partial \sigma_{st}} D_{stkl}^e & \text{Plastic.} \end{cases} \tag{10}$$

Loading condition will then take the following form

$$\max(\bar{\varphi}_1, \bar{\varphi}_2, \bar{\varphi}_3) \begin{cases} > 0 & \text{Loading,} \\ = 0 & \text{Neutral,} \\ < 0 & \text{Unloading,} \end{cases} \tag{11}$$

where

$$\bar{\varphi}_k = \frac{\partial \varphi_k}{\partial \sigma_{ij}} d\sigma_{ij}, \quad k = 1, 2, 3.$$

2.2. Multi-potential theory for jointed rock masses

Randomly distributed pre-existing microcracks in rock masses may usually affect the failure mode of jointed rock masses since fracturing often develops along these microcracks or interfaces. These phenomena were observed in a large number of failures of rock masses. Take the Malpassat arch dam for example, development of several arrays of pre-existing cracks in the bedrocks finally lead to the failure of the arch dam. Similar failure modes were also reported in laboratory tests of rock masses. It is assumed that pre-existing cracks can be generalized and described by three sets of dominant cracks, and then each of them can be associated with a potential function (in fact, the three functions correspond to yield surface in the classical elasto-plasticity).

It is worth noting that in case of 2-D problems, the number of sets of cracks, as well as that of potential functions, can be decreased to 2 thus the same to potential functions. Localization modes of the 2-D and 3-D specimen are shown in Figs. 1 and 2 respectively.

Three potential functions used to describe three dominant sets of cracks may take forms of the well-known Rankine or Mohr–Coulomb criteria. The Rankine criterion is defined as

$$\varphi_k = \sigma_1^{(k)} - \sigma_t^{(k)} = 0, \quad k = 1, 2, 3. \tag{12}$$

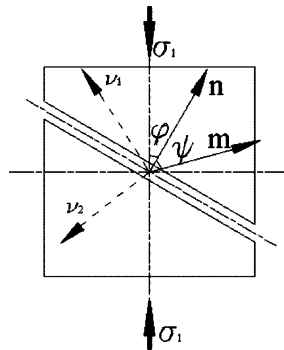


Fig. 1. Failure mode of uni-axial compression specimen.

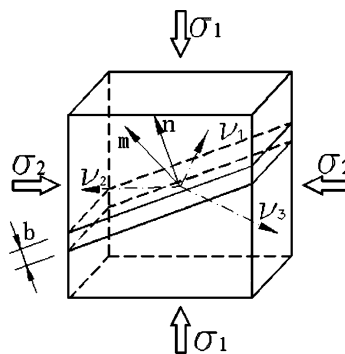


Fig. 2. Failure mode of 3-D specimen.

In the same way, those of Mohr–Coulomb criterion can be written as

$$\varphi_k = f_k \sigma^{(k)} + c_k - \tau^{(k)} = 0, \quad k = 1, 2, 3. \tag{13}$$

In the last two equations, $\sigma^{(k)} = v_i^{(k)} \sigma_{ij} v_j^{(k)}$, $\tau^{(k)} = \sqrt{\sigma_i^{(k)} \sigma_i^{(k)} - (\sigma^{(k)})^2}$, $\sigma_i^{(k)} = \sigma_{ij} v_j^{(k)}$, $v_i^{(k)}$ the unit normal vector of the k th generalized crack sets. f_k and c_k are frictional parameter and cohesive stress of the k th potential function respectively. By substituting these potential functions into Eqs. (10) and (11) respectively, the loading conditions and the tangent stiffness tensor can be obtained.

3. Bifurcation mode of localization for jointed rock masses

3.1. Conditions for bifurcation of localization

The emergence of localization in jointed rock masses can be characterized as the variance of behavior of the characteristic tangent stiffness tensor of rock masses. In order to analyze the localization in jointed rock masses, it is assumed that the current state of static equilibrium can be characterized in terms of continuous displacement u_i , stresses σ_{ij} and strains ε_{ij} . With increased loading it can be observed that discontinuous bifurcation of the rate of displacement gradient $\dot{u}_{i,j}$ may occur across a fixed singular surface Ω with orientation $n_i^{(x)}$ (unit vector) within the rock mass. Let x_i be the position on the singular surface. The displacement u_i remains continuous after the onset of localization, whereas the displacement gradient $\dot{u}_{i,j}$ will exhibit a jump across the singular surface, i.e.,

$$[\dot{u}_{i,j}] \equiv u_{i,j}^+ - u_{i,j}^- \neq 0 \tag{14}$$

in which $[\dot{u}_{i,j}] = \partial[\dot{u}_i]/\partial x_j$, “+” refers to the plus side of the plane of discontinuity and “-” to the minus side. According to Maxwell’s compatibility conditions, the rate of displacement gradient must satisfy the form

$$[\dot{u}_{i,j}] = c_i n_j, \tag{15}$$

where c_i is an arbitrary vector. According to the geometric relationship of the deformation, the jump of strain rate becomes

$$[\dot{\varepsilon}_{ij}] = \frac{1}{2}(c_i n_j + c_j n_i). \tag{16}$$

Define unit vector m_i as the orientation of c_i , i.e.,

$$m_i = c_i / |c|. \tag{17}$$

So the vectors \mathbf{n} and \mathbf{m} represent the orientation characters of the localization. There are three noteworthy extreme cases:

- (i) if $\mathbf{m} \cdot \mathbf{n} = 0$. The material in the band deforms in simple shear while a shear band develops.
- (ii) if $\mathbf{m} \cdot \mathbf{n} = 1$. The band undergoes extension normal to the planes of discontinuity. In certain circumstances this implies a splitting failure mode.
- (iii) if $\mathbf{m} \cdot \mathbf{n} = -1$. The band undergoes compression normal to the planes of discontinuity and the band will be a compaction one.

Equilibrium across the discontinuity planes requires that the tractions be continuous,

$$[\dot{\sigma}_{ij}] n_j = 0. \tag{18}$$

The tangent stiffness tensor D_{ijkl} will take the same value on both sides of the singular surface Ω , since $D_{ijkl} = D_{ijlk}$, from Eqs. (10), (16) and (17),

$$n_j D_{ijkl} n_k m_l = 0. \tag{19}$$

Define the characteristic tangent stiffness tensor \mathbf{T} as

$$\mathbf{T} = T_{il}(\mathbf{n}) = n_j D_{ijkl} n_k. \quad (20)$$

Then Eq. (19) becomes

$$T_{il}(\mathbf{n}) m_l = \mathbf{0}. \quad (21)$$

The onset of localization occurs at the first point in the deformation history of which a nontrivial solution of Eq. (21) exists. Therefore, the focus of the localization problem is then to determine the zero eigenvalue of tensor T_{il} , the possibility for localization is that

$$f(\mathbf{n}) = \det(T_{il}(\mathbf{n})) = 0. \quad (22)$$

3.2. Numerical method for localization direction

It is often difficult to obtain the analytical solution of vectors \mathbf{n} and \mathbf{m} from Eqs. (19) and (22). The nonlinear programming method for the eigenvalue problem is formulated here. According to the stiffness tensor, $D_{ijkl} = \lambda \delta_{ij} \delta_{kl} + \mu (\delta_{ik} \delta_{jl} + \delta_{il} \delta_{jk})$ for isotropic elastic materials, the function $f(\mathbf{n})$ can take the simple form

$$f(\mathbf{n}) = (\lambda + 2\mu) \mu^2, \quad (23)$$

where λ and μ are the Lamé constants of the virgin material. For isotropic elastic materials, the function $f(\mathbf{n})$ is always positive and independent of \mathbf{n} . In the process of continuous loading or deformation, properties of materials will degrade, and the value of the function may decrease. Finally the value of the function may become zero or even negative, which in turn indicates the onset of localization. In order to detect the variance of the signs of function $f(\mathbf{n})$, the minima of function for every increment of deformation should be computed and Eq. (22) be checked. This eventually results in considering the following nonlinear programming problem

$$\begin{cases} \min_{\mathbf{n}} f(\mathbf{n}) \equiv \det(T_{il}(\mathbf{n})) \\ \text{subjected to } |\mathbf{n}| = 1 \end{cases} \quad (24)$$

in which $T_{il}(\mathbf{n})$ is the characteristic tangent stiffness tensor of the current time.

Using Lagrange–Newton Method, the nonlinear programming problem in Eq. (24) can be formulated to the equivalent characteristic equation

$$\nabla f(\mathbf{n}) - \nabla |\mathbf{n}|^2 \Lambda = \nabla f(\mathbf{n}) - 2\Lambda n_i = 0, \quad (25)$$

where Λ is a Lagrange multiplier.

On substituting Eq. (22) into Eq. (25) leads to, then

$$\det(\mathbf{T}(\mathbf{n})) D_{ijkl} T_{kj}^{-1}(\mathbf{n}) n_l - \Lambda n_i = 0. \quad (26)$$

Denote the first term on the left hand of Eq. (26) as \mathbf{S} , i.e.,

$$S_{il}(\mathbf{n}) \equiv \det(\mathbf{T}(\mathbf{n})) D_{ijkl} T_{kj}^{-1}(\mathbf{n}). \quad (27)$$

Then Eq. (26) becomes

$$S_{il}(\mathbf{n}) n_l - \Lambda n_i = 0. \quad (28)$$

Two steps are needed to obtain the solution of Eq. (28):

- (a) For computing convenience, the direction vector \mathbf{n} is expressed in terms of spherical coordinates, namely,

$$\mathbf{n} = (\cos \phi \cos \theta, \cos \phi \sin \theta, \sin \phi). \tag{29}$$

Variations of ϕ and θ , which are limited from 0 to 2π and 0 to $\frac{1}{2}\pi$ respectively, are then scanned at a certain increment (say, 5°) to determine a preliminary approximation $\mathbf{n}^{(0)}$ to the minima.

- (b) By using the former approximation, the following iterative scheme can lead to the locations of the minima

$$S_{ii}(\mathbf{n}^{(k)})n_i^{(k+1)} - A^{(k+1)}n_i^{(k+1)} = 0. \tag{30}$$

Herein at each iteration an eigenvalue problem may be formed based on the matrix $\mathbf{S}(\mathbf{n}^{(k)})$ which is derived from the previous iteration of $\mathbf{n}^{(k)}$. Then the minimum eigenvector can be determined and taken as the new iterate $\mathbf{n}^{(k+1)}$. The step is repeated successively until the eigenvector converged within a given error.

Once the orientations of the localization band have been obtained, the corresponding vector \mathbf{m} can be determined from Eq. (21).

4. FEM implementation

In the following variational statement which includes the weak form of the strain–displacement equations, constitutive equations, equilibrium equations and static boundary conditions are implemented to discretize the problem

$$\int_V \delta \boldsymbol{\varepsilon}^T \tilde{\boldsymbol{\sigma}}(\boldsymbol{\varepsilon}) dV + \delta \int_V \boldsymbol{\sigma}^T (\partial \mathbf{u} - \boldsymbol{\varepsilon}) dV = \int_V \delta \mathbf{u}^T \bar{\mathbf{b}} dV + \int_{S_f} \delta \mathbf{u}^T \bar{\mathbf{t}} dS. \tag{31}$$

This variational equality must hold for any admissible variations $\delta \mathbf{u}$, $\delta \boldsymbol{\varepsilon}$ and $\delta \boldsymbol{\sigma}$. Herein, $\tilde{\boldsymbol{\sigma}}(\boldsymbol{\varepsilon})$ is the stress computed from the assumed strain through constitutive relationship, and ∂ is a kinematic operator which transforms displacements into strains, $\bar{\mathbf{b}}$ and $\bar{\mathbf{t}}$ are the prescribed forces and surface forces, respectively.

These unknown fields are interpolated as follows:

$$\mathbf{u} \approx \mathbf{N} \mathbf{d} + \mathbf{N}_c \mathbf{d}_c, \tag{32}$$

$$\boldsymbol{\varepsilon} \approx \mathbf{B} \mathbf{d} + \mathbf{G} \mathbf{e}, \tag{33}$$

$$\boldsymbol{\sigma} \approx \mathbf{S} \mathbf{s}, \tag{34}$$

herein \mathbf{N} is the standard displacement interpolation matrix, \mathbf{B} is the standard strain interpolation matrix, \mathbf{N}_c and \mathbf{G} are matrices containing some enhancement terms for displacements and strains respectively, \mathbf{S} is the stress interpolation matrix, \mathbf{d} , \mathbf{d}_c , \mathbf{e} and \mathbf{s} are degrees of freedom corresponding to nodal displacements, enhanced displacement modes, enhanced strain modes and stress parameters, respectively. The interpolation shown above can lead to a large number of special techniques beside the well-known B-bar approach.

By substituting equations from (32) to (34) into the variational equality, Eq. (31), and taking into account the independence of variations, these discretized equations can be obtained:

$$\int_V \mathbf{B}^T \tilde{\boldsymbol{\sigma}}(\mathbf{B} \mathbf{d} + \mathbf{G} \mathbf{e}) dV = \mathbf{f}_{\text{ext}}, \tag{35}$$

$$\int_V \mathbf{G}^T \tilde{\boldsymbol{\sigma}} (\mathbf{B}\mathbf{d} + \mathbf{G}\mathbf{e}) dV - \int_V \mathbf{G}^T \mathbf{S} dV \mathbf{s} = \mathbf{0}, \tag{36}$$

$$\int_V \mathbf{S}^T \mathbf{B}_c dV \mathbf{d}_c - \int_V \mathbf{S}^T \mathbf{G} dV \mathbf{e} = \mathbf{0}, \tag{37}$$

$$\int_V \mathbf{B}_c^T \mathbf{S} dV \mathbf{s} = \mathbf{0}, \tag{38}$$

where $\partial(\mathbf{N}\mathbf{d}) = \mathbf{B}\mathbf{d}$ and $\partial(\mathbf{N}_c\mathbf{d}) = \mathbf{B}_c\mathbf{d}$, \mathbf{B}_c is the strain interpolation matrix corresponding to the displacement interpolation \mathbf{N}_c . The vector of external forces $\mathbf{f}_{\text{ext}} = \int_V \mathbf{N}^T \bar{\mathbf{b}} dV + \int_{S_f} \mathbf{N}^T \bar{\mathbf{t}} dS$. The vector of nonstandard external forces, $\mathbf{f}_c = \int_V \mathbf{N}_c^T \bar{\mathbf{b}} dV + \int_{S_f} \mathbf{N}_c^T \bar{\mathbf{t}} dS$ may decrease to zero in the case of loads being assumed to be applied outside the region with enhanced interpolation.

The following stress–strain equation in the rate form is adopted to linearize the function of $\tilde{\boldsymbol{\sigma}}$ upon \mathbf{d} and \mathbf{e} ,

$$\dot{\tilde{\boldsymbol{\sigma}}} = \mathbf{D}\dot{\boldsymbol{\varepsilon}} \approx \mathbf{D}(\mathbf{B}\dot{\mathbf{d}} + \mathbf{G}\dot{\mathbf{e}}), \tag{39}$$

herein $\mathbf{D} \equiv \partial\tilde{\boldsymbol{\sigma}}/\partial\boldsymbol{\varepsilon}$ is the tangential stiffness matrix of the material. Substituting Eq. (39) into Eqs. (35)–(38) leads to a set of linear equations

$$\int_V \begin{bmatrix} \mathbf{B}^T \mathbf{D} \mathbf{B} & \mathbf{B}^T \mathbf{D} \mathbf{G} & \mathbf{0} & \mathbf{0} \\ \mathbf{G}^T \mathbf{D} \mathbf{B} & \mathbf{G}^T \mathbf{D} \mathbf{G} & -\mathbf{G}^T \mathbf{S} & \mathbf{0} \\ \mathbf{0} & -\mathbf{S}^T \mathbf{G} & \mathbf{0} & \mathbf{S}^T \mathbf{B}_c \\ \mathbf{0} & \mathbf{0} & \mathbf{B}_c^T \mathbf{S} & \mathbf{0} \end{bmatrix} dV \begin{Bmatrix} \dot{\mathbf{d}} \\ \dot{\mathbf{e}} \\ \dot{\mathbf{s}} \\ \dot{\mathbf{d}}_c \end{Bmatrix} = \begin{Bmatrix} \dot{\mathbf{f}}_{\text{ext}} \\ \mathbf{0} \\ \mathbf{0} \\ \mathbf{0} \end{Bmatrix}. \tag{40}$$

Since the interpolations of stress and strain may be in discontinuous forms, the interpolation functions can be properly selected such that each stress or strain parameter is associated with only one finite element. The same holds for the enhanced displacement parameters, so the parameters \mathbf{e} , \mathbf{s} and \mathbf{d}_c can be eliminated on the element level. thus the global equations contain only the standard displacement degree of freedom \mathbf{d} .

There are three basic types of approaches to simplify Eq. (40) with properly selected interpolation functions, see [5,18]. Eq. (40) will finally become

$$\begin{bmatrix} \mathbf{K}_{bb} & \mathbf{K}_{bg} \\ \mathbf{K}_{gb} & \mathbf{K}_{gg} \end{bmatrix} \begin{Bmatrix} \dot{\mathbf{d}} \\ \dot{\mathbf{e}} \end{Bmatrix} = \begin{Bmatrix} \dot{\mathbf{f}}_{\text{int}} \\ \mathbf{0} \end{Bmatrix}, \tag{41}$$

where $\mathbf{K}_{bb} = \int_{V_e} \mathbf{B}^T \mathbf{D} \mathbf{B} dV$, $\mathbf{K}_{bg} = \int_{V_e} \mathbf{B}^T \mathbf{D} \mathbf{G} dV$, $\mathbf{K}_{gb} = \int_{V_e} \mathbf{G}^T \mathbf{D} \mathbf{B} dV$, $\mathbf{K}_{gg} = \int_{V_e} \mathbf{G}^T \mathbf{D} \mathbf{G} dV$. $\dot{\mathbf{e}}$ can be eliminated supposed \mathbf{K}_{gg} is regular and written as

$$\dot{\mathbf{e}} = -\mathbf{K}_{gg}^{-1} \mathbf{K}_{gb} \dot{\mathbf{d}}. \tag{42}$$

Substituting Eq. (42) into Eq. (39) leads to

$$\dot{\boldsymbol{\varepsilon}} \approx \mathbf{B}\dot{\mathbf{d}} + \mathbf{G}\dot{\mathbf{e}} = \mathbf{B}\dot{\mathbf{d}} - \mathbf{G}\mathbf{K}_{gg}^{-1} \mathbf{K}_{gb} \dot{\mathbf{d}} = (\mathbf{B} - \mathbf{G}\mathbf{K}_{gg}^{-1} \mathbf{K}_{gb}) \dot{\mathbf{d}} \equiv \bar{\mathbf{B}}\dot{\mathbf{d}}, \tag{43}$$

where $\bar{\mathbf{B}} \equiv \mathbf{B} - \mathbf{G}\mathbf{K}_{gg}^{-1} \mathbf{K}_{gb}$ is the well-known B-bar matrix.

Then the element stiffness matrix can be written as

$$\mathbf{K} = \mathbf{K}_{bb} - \mathbf{K}_{bg} \mathbf{K}_{gg}^{-1} \mathbf{K}_{gb} = \int_{V_e} \bar{\mathbf{B}}^T \mathbf{D} \bar{\mathbf{B}} dV. \tag{44}$$

For elements satisfying the localization conditions in Section 3, the element stiffness matrix will be modified accordingly to consider the localization effects. This modification can be easily done in the standard FEM codes and thus enhanced the applicability of the FEM for localization problem.

5. Case studies

For a specimen with original imperfection, several studies were performed with two potential functions to simulate the localization of the material. Two functions adopted are Rankine criterion and Mohr–Coulomb criterion as in Eqs. (29) and (30) (it should be noted that number k equals 2 for 2-D problem and 3 for 3-D problems).

As for Rankine criterion, namely maximum tension cut-off criterion, the potential function is defined by

$$\varphi_k = \sigma_1^{(k)} - \sigma_t^{(k)} = 0, \quad k = 1, 2. \quad (45)$$

For Mohr–Coulomb criterion, its potential function is

$$\varphi_k = f_k \sigma^{(k)} + c_k - \tau^{(k)} = 0, \quad k = 1, 2. \quad (46)$$

FEM analysis were performed for specimens with the above two criterion. The input data for this model used in this study are shown as follows, initial elastic modulus $E = 30$ GPa, Poisson's ratio $\mu = 0.2$. Other parameters for the model are given here: $\sigma_t^1 = 3.36$ MPa, $\sigma_t^2 = 3.60$ MPa, $f_1 = \tan 30^\circ$, $f_2 = \tan 35^\circ$, $c_1 = 0.80$ MPa, $c_2 = 0.90$ MPa. With these two potential functions, several studies were performed for test specimens. These include specimens under tension or compression.

5.1. Original imperfections on the upper edge

The original shape of the specimen is shown in Fig. 3, with left edge horizontally constrained and bottom vertically constrained. The 2-D FEM mesh consists of 8×7 elements embedded with discontinuity. The displacement load is exerted on the right edge. In order to demonstrate the effects of the imperfection to the localization bands, different positions of imperfection in the specimen were set, namely on the upper-left corner, upper-right corner and both upper corner of the upper side.

If there is original imperfection on the upper-right corner, the shear band as shown in Fig. 4 will emerge within the specimen. As can be seen from the figure, localization band will be triggered from the imperfection and form a nearly diagonal band in the specimen. If there is original imperfection on the upper-left corner, the shear band within the specimen is shown in Fig. 5, also a nearly diagonal band starting from the imperfection in the upper-left corner. If original imperfections are on both corners of the upper edge, then two localization bands in two diagonal will form in the specimen as demonstrated in Fig. 6.

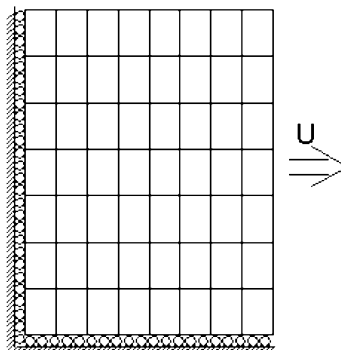


Fig. 3. Original mesh of the specimen.

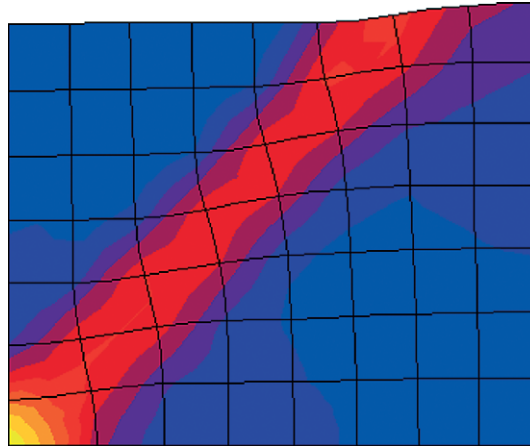


Fig. 4. Localization: imperfection on upper-right corner.

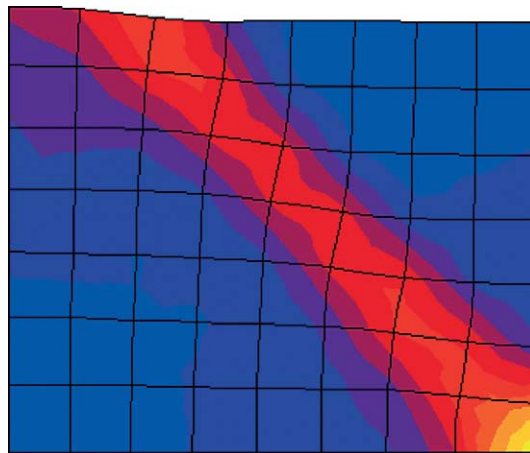


Fig. 5. Localization: imperfection on upper-left corner.

5.2. Specimen with randomly distributed microcracks

Different ratios of vertical and horizontal displacements, say, different U_v/U_h were applied on the upper and right side of the 2-D specimen within which the distributed microcracks were distributed randomly. The FEM mesh for the specimen, consisting of 80×150 elements, is shown in Fig. 7. The vertical and horizontal displacement U_v and U_h increments prescribed as displacement load were increased in certain proportions as $1/0$, $5/1$, $1/1$, $-1/0$, $-5/-1$ and $-1/-1$. The first three cases correspond to tensile load on one or two sides of the specimen, while the latter three correspond to compression load on the sides.

The localization results for tension are shown in Figs. 8–10. In the uni-axial tension case, namely $U_v/U_h = 1/0$, the localization band is nearly perpendicular to the maximum principal stress, i.e., the direction of the tensile load. This case was demonstrated in Fig. 8. When tensile load is put on the horizontal side of the specimen, another localization band fainter than the former one nearly in the diagonal line of the specimen was observed in the results shown in Fig. 9. Furthermore, when the ratio of the horizontal load increases, a notable localization band appears with the former one, shown in Fig. 10.

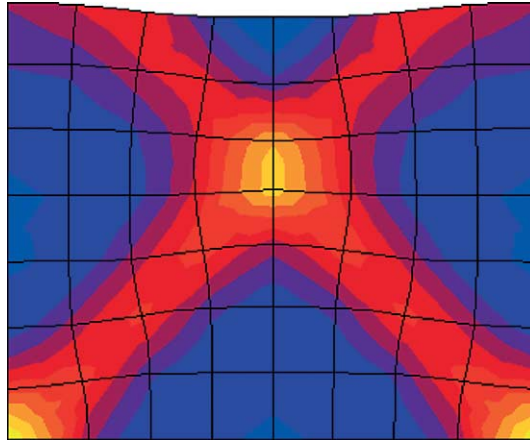


Fig. 6. Localization: imperfection on upper corners.

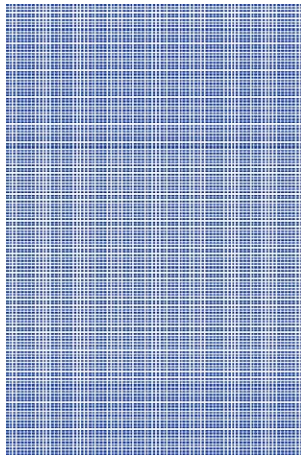
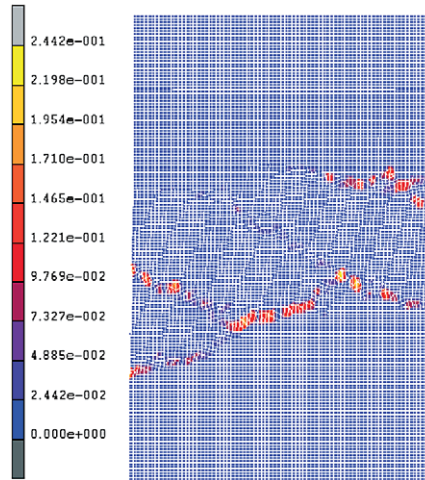
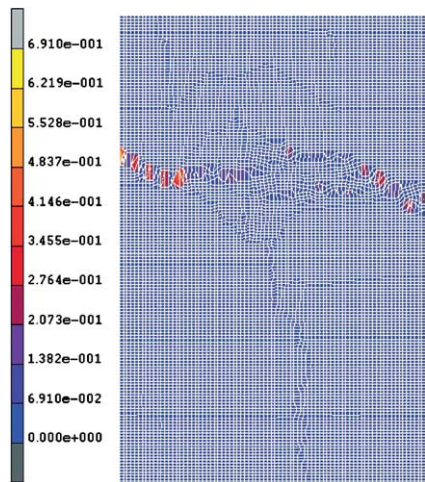


Fig. 7. FEM mesh of specimen.

Under compression, localization was detected only when the ratio of U_v to U_h equals $-1/0$, which is shown in Fig. 11. Different from the pure compaction band perpendicular to the compression stress on the vertical side, the localization band emerges with a certain angle to the horizontal line. The band is a compacting and shearing one. No localization was detected for other two ratios.

6. Engineering case

Xiluodu arch dam to be located on the upper stream of Jinsha River in southwest China, one of the main tributaries of Yangtze River, is under construction now. The double curvature arch dam is designed to be 278 m high and will be constructed on complex rock formations with developed horizontal faults and fissures. Characterized data of the Xiluodu project is listed in Table 1. Three-dimensional FEM computation was performed using the multi-potential model of discontinuous bifurcation proposed in this paper

Fig. 8. Localization results when $U_v/U_h = 1/0$.Fig. 9. Localization results when $U_v/U_h = 5/1$.

in order to simulate the complex geological and fracture conditions in the bedrock masses. Altogether 9852 elements containing 11,558 nodes are simulated, and among them, 270 elements are dam body elements. There are 11 different materials whose parameters are set to account for the complicated geological conditions, including several horizontal large faults and millions of microfracture in the bed rock mass. Fig. 12 shows the coarse 3-D FEM mesh of the arch dam for the localization analysis.

Physical modeling tests, a rupture model test in order to find the limit capacity of the resistance dam structure under static structural loads and to simulate its ultimate failure modes, have been conducted recently. The models were reproduced to simulate the dam itself, with the dam geological formations including several large faults and rock joints. The model scale is 1:250.

A comparison between failure patterns of the dam from both numerical analysis and the physical rupture modeling tests with the overloading of upstream water pressure has been made to evaluate its safety

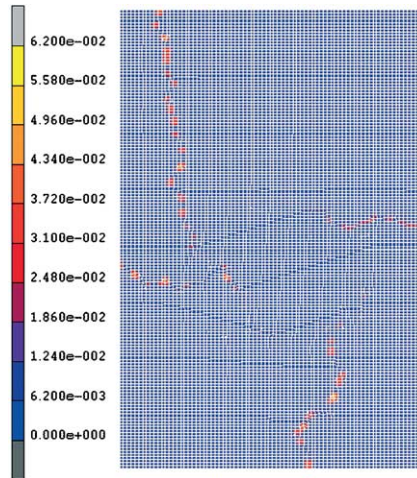


Fig. 10. Localization results when $U_v/U_h = 1/1$.

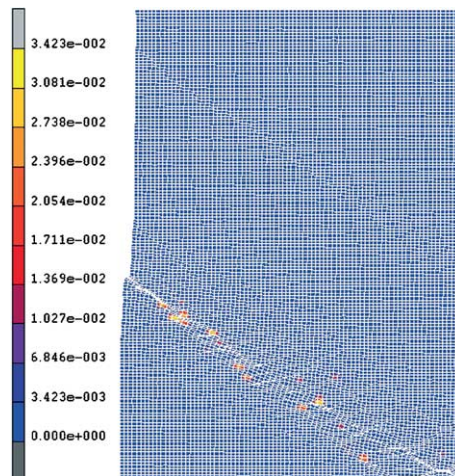


Fig. 11. Localization results when $U_v/U_h = -1/0$.

and stability. The failure pattern of the arch dam from numerical analysis is shown in Fig. 13 with seven times upstream water pressure overloading. Fig. 14 shows the results from physical modeling tests with seven times upstream water pressure overloading. The failure pattern of the arch dam from numerical simulation is in approximately agreement with that of the physical modeling tests.

7. Conclusion

In this paper, damage localization is analyzed as discontinuous bifurcation based on the mechanisms of localization of jointed rock masses in the framework of multi-potential theory. In order to obtain the localization orientation, a numerical method was used to compute the solution of the eigenvalue problem

Table 1
Characterized data of the Xiluodu project

<i>Xiluodu project</i>	
Location	Jinsha River, Sichuan, China
Main function	Power generation
Total installed capacity	14,400 MW
Annual power output	63,010 GW h
Project configuration	Arch dam, water releasing structure, diversion channel, switch station, log-passing system, secondary dam
<i>Dam body</i>	
Dam type	Double curvature arch dam
Max. height	278 m
Crest length	841 m
Thickness at the base of crown	14 m
Thickness at the top of crown	69 m
Max. central angle of arch (left bank)	48.74°
Max. central angle of arch (right bank)	47.44°
Upstream curvature radii range (right bank/left bank)	236.91–512.49 m/241.51–419.16 m
Downstream curvature radii range (right bank/left bank)	150.82–271.15 m/94.46–270.02 m

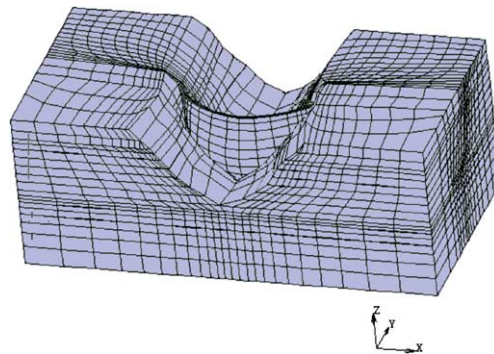


Fig. 12. Coarse FEM mesh of Xiluodu arch dam.

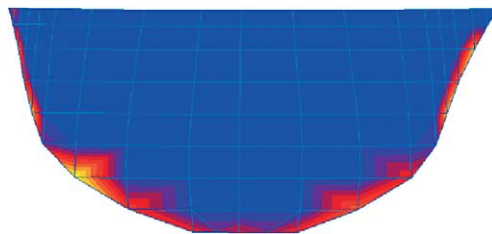


Fig. 13. Localization results from numerical analysis with seven times upstream water pressure overloading.

resulting from the bifurcation model. To take into account the effect of localization, elements embedded with discontinuous deformation were adopted and corresponding codes were designed into standard FEM program. With the aid of the enhanced FEM program, localizations in several specimens were studied in this paper. Xiluodu arch dam also serves as an example for numerical analysis. Numerical results of the arch dam are coincided very well with those of the physical modeling tests.

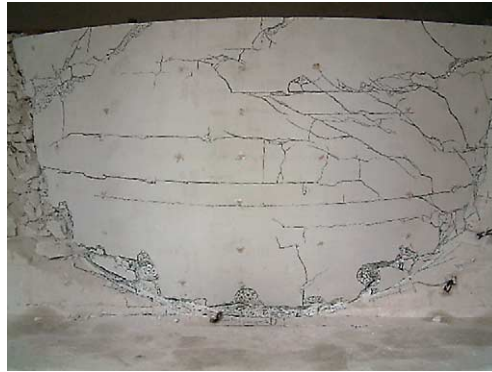


Fig. 14. Failure of upstream of Xiluodu arch dam with seven times upstream water pressure overloading (physical modeling test).

Acknowledgements

This study was jointly financially sponsored by NSFC (the National Science Foundation of China) with grant no. 59939190 and Schlumberger BGC. The authors would like to thank Professor R.Q. Yang and D.L. Shen for their technical endeavor in the physical modeling tests of this study. The second author wants to convey his thanks to Dr. Guanglin Du and Dr. Yaoru Liu for their help and instructive discussion.

References

- [1] T. Belytschko, J. Fish, B.E. Engelmann, A finite element with embedded localization zones, *Comput. Methods Appl. Mech. Engrg.* 70 (1988) 59–89.
- [2] E.N. Dvorkin, A.M. Cuitiño, G. Gioia, Finite elements with displacement interpolated embedded localization lines insensitive to mesh size and distortions, *Int. J. Numer. Methods Engrg.* 30 (1990) 541–564.
- [3] J. Fish, T. Belytschko, Elements with embedded localization zones for large deformation problems, *Comput. Struct.* 30 (1988) 247–256.
- [4] R. Hill, J.W. Hutchinson, Bifurcation phenomena in the plane tension test, *J. Mech. Phys. Solids* 23 (1975) 239–264.
- [5] M. Jirásek, Comparative study on finite elements with embedded discontinuities, *Comput. Methods Appl. Mech. Engrg.* 188 (2000) 307–330.
- [6] M. Klisinski, K. Runesson, S. Sture, Finite element with inner softening band, *J. Engrg. Mech. ASCE* 117 (1991) 575–587.
- [7] P.V. Lade, Elasto-plastic stress–strain theory for cohesionless soil with curved yield surface, *Int. J. Solids Struct.* 13 (1977).
- [8] R. Larsson, K. Runesson, Discontinuous displacement approximation for capturing plastic localization, *Int. J. Numer. Methods Engrg.* 36 (1993) 2087–2105.
- [9] R. Larsson, K. Runesson, Element-embedded localization band based on regularized displacement discontinuity, *J. Engrg. Mech. ASCE* 122 (1996) 402–411.
- [10] J. Oliver, Modelling strong discontinuities in solid mechanics via strain softening constitutive equations. Part 1: Fundamentals. Part 2: Numerical simulation, *Int. J. Numer. Methods Engrg.* 39 (1996) 3575–3624.
- [11] M. Ortiz, An analytical study of the localized failure modes of concrete, *Mech. Mater.* 6 (1987) 159–174.
- [12] M. Ortiz, Y. Leroy, A. Needleman, A finite element method for localized failure analysis, *Comput. Methods Appl. Mech. Engrg.* 61 (1987) 189–214.
- [13] N.S. Ottosen, K. Runesson, Properties of discontinuous bifurcation solutions in elasto-plasticity, *Int. J. Solids Struct.* 27 (4) (1991) 401–421.
- [14] J.H. Prvost, K. Hoeg, Effective stress–strain model for soils, *J. Geotech. Engrg. Div., ASCE* 101 (1975).
- [15] J.W. Rudnicki, J.R. Rice, Conditions for the localization of deformation in pressure-sensitive dilatant materials, *J. Mech. Phys. Solids* 23 (1975) 371–394.
- [16] S. Ohmaki, A mechanical model for the consolidated cohesive soil, *Soils Found.* 19 (1979).
- [17] Z. Shen, A stress–strain constitution model of soil with three yield surfaces, *Chin. J. Solid Mech.* 5 (2) (1984) 163–174 (in Chinese).

- [18] J.C. Simo, J. Oliver, A new approach to the analysis and simulation of strain softening in solids, in: Z.P. Bažant (Ed.), *Fracture and Damage in Quasibrittle Structures*, E. and F.N. Spon, London, 1994, pp. 25–39.
- [19] J.C. Simo, J. Oliver, F. Armero, An analysis of strong discontinuities induced by strain softening in rate-independent inelastic solids, *Comput. Mech.* 12 (1993) 277–296.
- [20] G. Yang, The mathematical theory for the constitutive model of soils and its application, Ph.D. Thesis, Department of Hydraulic Engineering, Tsinghua University, 1998 (in Chinese).
- [21] Z. Yin, A twofold-yield-surface stress–strain model for soil masses, *Chin. J. Geo-Engrg.* 10 (4) (1988) 64–71 (in Chinese).